MEMS-Based Nanomechanics: Influence of MEMS Design on Test Temperature

**B. Pant · S. Choi · E.K. Baumert · B.L. Allen ·
S. Graham · K. Gall · O.N. Pierron**

Abstract Microelectromechanical system (MEMS) devices based on electro-thermal actuation have been used over the past few years to perform tensile tests on nanomaterials. However, previous MEMS designs only allowed small (*e.g.*, <100 nm) total displacement range without a significant increase in temperature near the nanospecimens (<20°C), thereby limiting the design of the load sensor or the range of nanomaterials to test. Here we characterize the thermo-mechanical behavior of three MEMS devices, using optical displacement measurements, micro-Raman temperature measurements, and finite element modeling. We observe the increase in temperature near the nanospecimen gap per displacement of thermal actuator to linearly decrease with the distance between nanospecimen gap and thermal actuator. We also present a MEMS device that can provide up to 1.6 μm of total displacement with less than 10°C increase in temperature near the nanospecimens, more than one order of magnitude improvement with respect to previously published MEMS material testing setups. This MEMS device can be used for accurate, temperature-controlled tensile testing of nanocrystalline metallic nanobeams.

Keywords MEMS · Nanomechanics ·
Nanocrystalline metals

B. Pant · S. Choi · E.K. Baumert · B.L. Allen · S. Graham ·
K. Gall · O.N. Pierron (✉)
G.W. Woodruff School of Mechanical Engineering,
Georgia Institute of Technology,
Atlanta, GA 30332-0405, USA
e-mail: olivier.pierron@me.gatech.edu

Introduction

Experimental nanomechanics is a growing research field motivated by the engineering need to characterize the mechanical properties of one-dimensional nanostructures, and by the scientific goal to understand and predict the governing size effects at the nanoscale [1–18]. As such, experimental techniques have been developed to enable nanoscale specimen testing, including atomic force microscopy [13, 15], nano/pico indenter based techniques [4, 12, 16, 19], and microelectromechanical system (MEMS) based techniques [6, 7, 14, 20–28]. MEMS based techniques are inherently well suited for nanomechanical tests, offering a micron-scale "lab-on-a-chip" setup [29].

Two types of on-chip actuation are commonly used in MEMS devices: electrostatic and thermal. Thermal actuators can provide larger displacements (several μm)/forces (several mN) than electrostatic (comb drive) actuators for the same size, an advantage when the MEMS footprint is a concern (*e.g.* for *in-situ* TEM tests [2, 3, 22]). However, since Joule heating and the resulting thermal expansion of beams is the basic principle of electro-thermal actuators, it is necessary to carefully monitor the actual MEMS temperature near the nanospecimens [14, 21, 27, 28]. For example, Zhu et al. concluded that the total actuator displacement for their MEMS devices should not exceed 100 nm to limit the temperature increase near the specimen to less than 20°C [21]. While an actuator displacement of 100 nm may be sufficient for some types of nanomaterials, it certainly limits the usable range of the thermal actuator, and therefore adds more constraints to the design of the load sensing part of the MEMS device. This coupling between temperature and specimen elongation can also be

detrimental to the interpretation of the results for certain classes of materials, such as metallic nanowires. Indeed, Zhu et al. predicted a significant temperature dependence on dislocation nucleation stress for Cu nanopillars (~700 MPa decrease in yield stress for an increase of 100°C), due to the small activation volumes associated with dislocation-based plasticity at this scale [30].

It is therefore the goal of this paper to present a thermal-actuator-based MEMS device for nanomechanical testing that provides a *large range of actuator displacement (~1– 2μm) with no appreciable increase in temperature of the nanospecimens*. For this purpose, three MEMS designs were thoroughly characterized based on experimental measurements of actuator displacement and temperatures as well as finite element simulations. We also present a tensile test to failure of a nanocrystalline Ni nanobeam to highlight the feasibility of performing nanotensile tests at constant temperature with our improved MEMS device.

Description of the MEMS Devices

The MEMS devices were fabricated with the SOIMUMPS process (MEMSCAP) [31], which relies on the bulk micromachining of a silicon-on-insulator (SOI) wafer. The single-crystal silicon (Si) structural layer is 10 μm thick (±1 μm), and is isolated from the substrate by a 1-μm-thick oxide layer (±0.05 μm). The surface of the Si layer is highly doped with phosphorous. The metallic pads consist of 500 nm gold with a 20 nm chrome adhesion layer. This process allows the fabrication of through-hole devices, a necessary feature for *in-situ* TEM testing (see Fig. 1).

Three MEMS designs (D1, D2, D3) were investigated in this study (see Fig. 2). The devices exhibit a similar architecture: an electrothermal actuator (ETA), a heat sink, a gap for the nanospecimens, and a capacitive load sensor. The thermal actuator consists of 10 pairs of beams (4 μm wide) inclined at 5°. The load sensor is made of 4 beams deforming in bending mode. The beams are 500 μm long and 9 or 21 μm wide. The amount of deformation of the beams is measured with a comb structure, consisting of 21
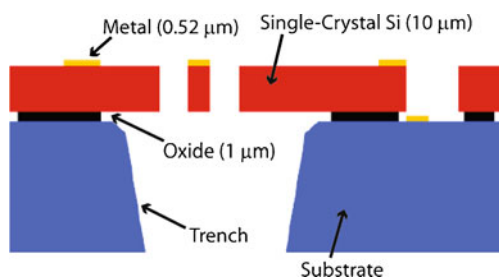
pairs of combs on each side of the device's symmetry axis. The air gaps on each side of the combs are 4 and 9 μm; the 2.5 μm offset in air gap increases the sensitivity of the capacitance measurements for small deflections. The displacements can be measured with a universal capacitive readout IC chip (MS3110, Irvine Sensor) [20, 22, 23, 26, 32].

The first two designs (D1 and D2) differ primarily by their heat sink geometry. D1 MEMS devices have the smallest footprint and are 1 mm long and 1.3 mm wide; the heat sink consists of a large area of Si (38 μm by 580 μm) designed to increase heat transfer with the surrounding air. The distance between the hot actuation beams and the nanospecimen is 70 μm. D2 devices have a larger heat sink (115 μm by 580 μm) than D1. In addition, a pair of beams connected to large metallic pads on the sides was added in between the heat sink and the specimen gap.[1] The distance between the hot actuation beams and the nanospecimen is 250 μm. D3 devices are substantially different from D1 and D2; they are 3.5 mm long and 1.5 mm wide. Unlike D1 and D2 devices that have only one comb structure for load sensing purposes, D3 devices have two identical comb structures placed on each side of the nano-specimen gap. These two comb structures can be used to electronically measure the gap change during a test (and hence the nanospecimen elongation) with the MS3110 chip [32]. D3 devices are also mechanically disconnected at two other locations than the specimen gap. These extra 4-μm gaps are filled with stiff, electrically insulating epoxy, which was applied using a micromanipulator needle under a probe station and was cured at room temperature for 24 h. These epoxy links allow the necessary electrical isolation between the driving and sensing part of the MEMS device for proper sensing while maintaining mechanical connectivity.[2] The heat sink is also larger; including the heat sink and the capacitive sensor, the distance between the thermal actuator and the nanospecimen is 1.5 mm.

Governing Equations of the MEMS Devices

The governing equations of the MEMS devices are derived based on the lumped mechanical model shown in Fig. 2:

$$X_A = X_S + X_{LS} = X_{S,el} + X_{S,pl} + X_{LS} \tag{1}$$

$$F = K_{LS}X_{LS} = K_S X_{S,el} \tag{2}$$

Fig. 1 Schematic cross-section showing general features of a SOIMUMPs structure

---

[1] The beams were added to allow the resistance measurement of a nanospecimen during a test (via a 2 terminal setup).
[2] Given the large area of the epoxy link, and the expected elastic modulus of several GPa, the stiffness of the epoxy should be 2 to 3 orders of magnitude larger than the stiffness of the load sensor or nanospecimen. Hence the epoxy links do not affect the overall mechanics of the MEMS device.

Fig. 2 Optical and SEM images of the three MEMS designs: **(a)** D1; **(b)**: D2; **(c)**: D3; *ETA* electrothermal actuator, *CS* comb structure, *HS* heat sink, *NG* nanospecimen gap. **(d)** Equivalent lumped model for D1 and D2. The lumped model for D1 and D2 can be extended to D3 by simply redefining the actuator attributes. K_A and X_A in the equivalent lumped model for D3 represent the combined attributes of ETA and CS1
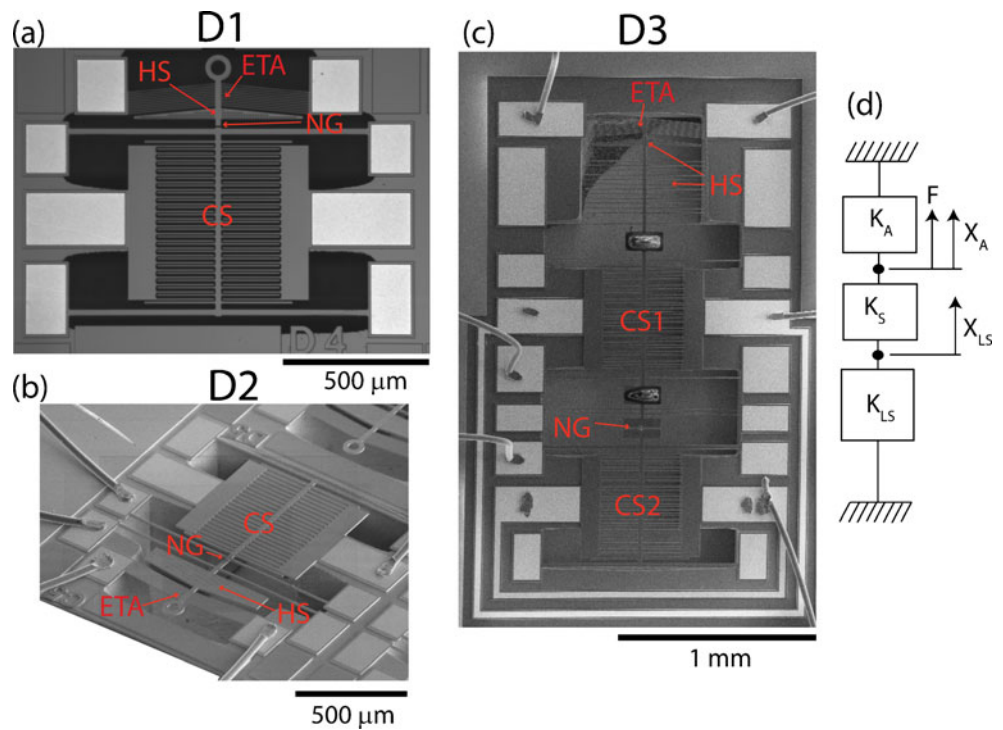
where X_A is the actuator displacement, X_S is the elongation of the specimen ($X_{S,el}$ is the elastic part and $X_{S,pl}$ is the plastic part of the specimen elongation), X_{LS} is the deflection of the load sensor, F is the force applied on the specimen and the load sensor, K_{LS} is the load sensor stiffness and K_S is the specimen stiffness. During a test, X_A can be assumed to equal the load-free actuator displacement, $X_A^{F=0}$, provided K_{LS} and K_S are small compared to the thermal actuator stiffness, K_{TA}; otherwise the relationship between X_A and $X_A^{F=0}$ is [21]:

$$X_A = X_A^{F=0} - \frac{F}{K_{TA}} = X_A^{F=0} - \frac{K_{LS}X_{LS}}{K_{TA}} = X_A^{F=0} - \frac{K_S X_S}{K_{TA}}$$

(3)

Assuming that K_{LS} is negligible compared to K_S, we have $X_{LS} \sim X_A$, hence equation (3) becomes:

$$X_A \approx \frac{X_A^{F=0}}{1 + \frac{K_{LS}}{K_{TA}}}$$

(4)

The thermal actuator stiffness, K_{TA}, can be approximated as [21]:

$$K_{TA} = 20\left(\sin^2\theta + \frac{\cos^2\theta}{\psi}\right)\frac{EA}{l}$$

(5)

with $\psi = \dfrac{Al^2}{12I} = \dfrac{l^2}{h^2 + b^2}$

(6)

with θ the beam angle, E the elastic modulus, A the cross-sectional area, l the beam length, I the moment of inertia of the cross-section with respect to the out-of-plane axis, h the beam thickness, and b the beam width.

Experimental Measurements

Thermal Actuator Displacements

The displacement of the thermal actuators operated in air was measured using a high magnification optical system (In-line assembly consisting of an Infinitube™ FM with 100X Mitutoyo M Plan Apo objective, and a Pulnix TMC-1400CL monochrome camera (pixel size 4.6 by 4.6 μm)) and a MATLAB routine. The resolution of the technique is limited by the pixel size (46 nm at 100X magnification) and is below the spatial resolution associated with optical diffraction (~200–300 nm). The reason for the pixel resolution is that a gap *change* is measured, not an absolute distance (which would be limited by optical diffraction). Consider a large gap (several microns in length) surrounded by two objects, and the corresponding intensity profile. The intensity varies near the edges due to optical diffraction. Assume one object moves by a distance d from the other. Since the actual gap is much larger than the distance affected by diffraction, the intensity profile near the edge of the object is unchanged by the object movement. The shift in intensity profile, equal to the gap change, can be measured with a pixel resolution, as explained next.

Practically, a MEMS device whose specimen gap was glued with stiff epoxy was used for the optical calibration. Optical images of the comb structure were taken at a 100X magnification for a series of DC voltages applied to the thermal actuator (from 0 to 4 V, in 0.2 V increment). The features of interest were a fixed comb, an adjacent moving comb, and the gap in between. A MATLAB routine was created to measure relevant distances from the images. First, the grayscale images were converted to binary images using the *im2bw* function. The intensity threshold was determined using the *graythresh* function. The binary images were then used to measure the number of pixels between the centers of both comb beams (see Fig. 3). Specifically, a routine was implemented to find the edges of the combs based on the value of the pixel: 0 (gap) or 1 (Si). This process was repeated for ~100 vertical lines perpendicular to the comb edges. The width of the beams and distance between the beams' centers (in number of pixels) were then measured and averaged based on the position of the beams' edges. The results were then corrected for any angle between the beams and the horizontal. The distance between the beam centers at zero driving voltage is accurately known (10 μm) since it is a periodic pattern, and was used to calculate the pixel size (which was found to be exactly 46 nm, the pixel size at 100 X magnification according to the camera specifications).

MEMS Temperature

Micro-Raman spectroscopy measurements were performed using a Renishaw inVia Raman Microscope to measure
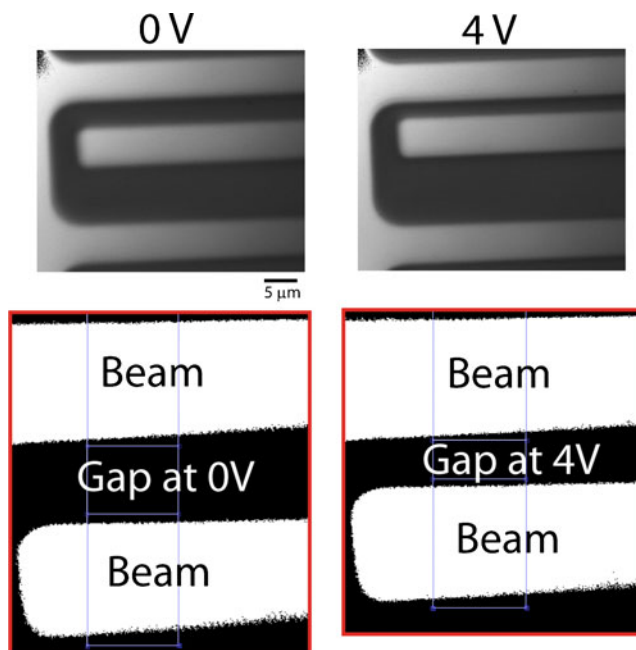
Fig. 3 Optical images at 100X magnification and corresponding binary images used for measuring ETA displacement

temperatures at specific locations of the MEMS device during operation. Raman measurements were carried out with 180° backscattering configuration and un-polarized detection. A 488 nm Ar-laser was employed as the excitation source. The laser power was adjusted to approximately 1.0 mW to prevent localized laser heating by laser light absorption. The shift in Stokes Raman peak position (~520 cm^{-1}) was utilized for temperature measurement. Since the MEMS structures were free standing and made of a single layer of monocrystalline Si, temperature induced stress contributions to the Stokes peak shift could be neglected [33]. The spatial resolution of the technique was limited by the laser spot diameter (~1 μm). To obtain phonon frequency maps and therefore temperature maps, Raman Stokes signals were collected while the actuator was heated up in an isothermal environment to known temperatures (21.3, 50, 100, 150, 200, 250°C). Then measurements were made near the specimen gap on the actuator side of the MEMS devices for a series of applied DC voltages across the thermal actuator (0, 1, 2, 3, 4 V). Best estimates and uncertainties (95% confidence bounds) of temperatures were calculated based on 10 measurements at each condition. The uncertainty in the temperature measurements is approximately ±1.5°C.

Finite Element Simulations

Thermal actuators have already been thoroughly modeled numerically, and the salient features for proper modeling highlighted [34, 35]. Here, a 3D finite element model of our thermal actuators was performed (using Ansys 12.0.1) and directly compared to our experimental results (thermal actuator displacement, temperature near specimen gap). Specifically, a coupled electrical-thermal-structural (multiphysics) analysis was done to determine the actuator displacement and temperatures as a function of applied driving voltages. Due to symmetry, only half the actuator was modeled to decrease the computational time. The model included the thermal actuator (10 μm thick monocrystalline Si layer) and the heat sink as well as the 500 μm thick air cushion between the device and the substrate (to account for conductive heat transfer). Convective heat transfer through the air was also modeled, while radiative heat transfer was ignored due to the low temperatures (<500 K) attained in the studied regime. Design D3 was not modeled since the thermophysical properties of the epoxy glue used for electrical insulation (see Fig. 2) could not be accurately determined.

SOLID227 elements were used to perform the coupled analysis. The boundary conditions were as follows. At the symmetry plane the displacement and heat flow normal to the symmetry plane acted symmetrically, while the voltage was taken to be zero for the actuator. In addition, for the electrical domain, the voltage was set to V$_{total}$/2 on the

actuator pad. For the thermal domain, it was assumed that the temperature on the actuator pad was set at room temperature (298 K) along with the lower face of the air block (substrate). All the displacements were set to zero on the actuator pad and the stiffness beam pad for the structural boundary. Mesh refinement was done until convergence of the results was achieved.

The following material properties were employed. First, the Si film was modeled as two different layers to account for the surface doping. The bottom layer is n-type with a resistivity of 10Ω-cm [31]. The top layer was n^+-type Si and the resistivity of that layer (assumed to be 2 μm) was calculated based on the total actuator resistance measured experimentally (typical value for actuator resistance ~100 Ω). Changing the thickness of the n^+-type layer (and therefore its resistivity to get the same total resistance) did not affect the results significantly (less than 1% difference in displacement). The resistivity of both layers was assumed to be temperature independent, since the measured resistance of the thermal actuators was fairly constant for the studied range of displacement. In contrast, the influence of temperature on the coefficient of linear thermal expansion and thermal conductivity of Si was taken into account (see Table 1) [35]. Thermal conductivity of air used was 0.026 W.m^{-1}.K^{-1} [34]. Convection heat transfer coefficients for air were varied between 10 and 100 W.m^{-2}.K^{-1} [35]. Finally the orthotropic properties of single crystal Si oriented in the <110>direction of the (100) plane were used [36].

The stiffness of the load sensor was also numerically modeled. Since only the four beams contribute to the stiffness of the load sensor, the comb structure for capacitive sensing was excluded from the model to minimize computational time. The mesh was made of SOLID 187 elements. The ends of the beams connected to the substrate were assumed to be fixed. The deflection obtained for a small applied force to the actuator was used to calculate the stiffness of the load sensor. Mesh refinement was done until convergence of the results was achieved. The effect of nonlinearities on the load sensor stiffness was also investigated (using NLGEOM function) to

Table 1 Variation of coefficient of linear thermal expansion α and thermal conductivity k_t with temperature. Based on [35]

Temperature (K)	k_t (W m^{-1} K^{-1})	α (μm m^{-1} K^{-1})
300	146.4	2.568
400	98.3	3.212
500	73.2	3.594
600	57.5	3.831
700	49.2	3.987
800	41.8	4.099
900	37.6	4.185

ensure accurate force calculations in case of large load sensor deflections.

Results and Interpretation

### Effect of MEMS Design on Thermal Actuator Behavior

Figure 4 shows a comparison of the experimental and finite element results for the D1 and D2 devices operating in air. The temperature of the MEMS device near the nanospecimens (Fig. 4(b)) and the thermal actuator displacement (Fig. 4(a)) are plotted as a function of driving voltage between 0 and 3 V. The numerical results (temperature and displacement) match closely the experimental data for two different designs, thereby validating the accuracy of our finite element model. According to these results, the effect of the change in heat sink geometry between D1 and D2 is to decrease the MEMS temperature near the nanospecimen as well as the resulting displacement. At 3 V, the displacement is ~0.9 μm for D1 and ~0.75 μm for D2, while the MEMS temperature near the nanospecimen is 140°C for D1 and 100°C for D2. The lower displacement for D2 is a result of lower temperatures attained by the actuator beams (146°C for D1 vs. 131°C for D2). D1 and D2 are, however, similar in the context of performing tensile tests of nanospecimens at constant temperature. Figure 4(c) shows that both designs exhibit a similar increase in temperature near the specimen gap per displacement of the thermal actuator (1.3°C/10 nm for D1, compared to 1.1°C/10 nm for D2). In both cases, the maximum allowable MEMS actuator displacement is slightly less than 100 nm to limit the temperature increase to 10°C, which does not represent a significant improvement compared to other existing MEMS material testing systems (100 nm for a 20°C increase) [21].

In contrast to D1 and D2 devices, D3 devices exhibit an order of magnitude lower increase in temperature near the specimen gap per displacement of the thermal actuator (0.07°C/10 nm for D3, compared to 1.3 and 1.1°C/10 nm for D1 and D2, respectively). According to Fig. 4(d), the temperature increase near the specimen gap per displacement of thermal actuator is linearly related to the distance between nanospecimen and thermal actuator. The significant improvement in the behavior of D3 devices therefore appears to mainly result from the larger distance between the nanospecimen and the thermal actuator (1.5 mm for D3, 250 μm for D2, and 70 μm for D1), even though additional factors may contribute to that effect, such as the beneficial effect of the low thermal conductivity of the epoxy (not studied here). We conclude that D3 devices can provide a displacement of 1.6 μm for a temperature increase of only 10°C near the nanospecimen. We also note that, while the footprint for the D3 devices is almost three times that of D1

Fig. 4 (a) ETA displacement (in air) *vs.* applied voltage, and (b) temperature near nanospecimen gap (in air) *vs.* applied voltage for the three MEMS designs. Experimental measurements and numerical calculations (FEM) are compared for D1 and D2. (c) Temperature near nanospecimen gap *vs.* ETA displacement for the three MEMS designs. (d) Average increase in temperature near nanospecimen per 10 nm of ETA displacement (slopes from (c)) *vs.* distance between ETA and nanospecimen gap
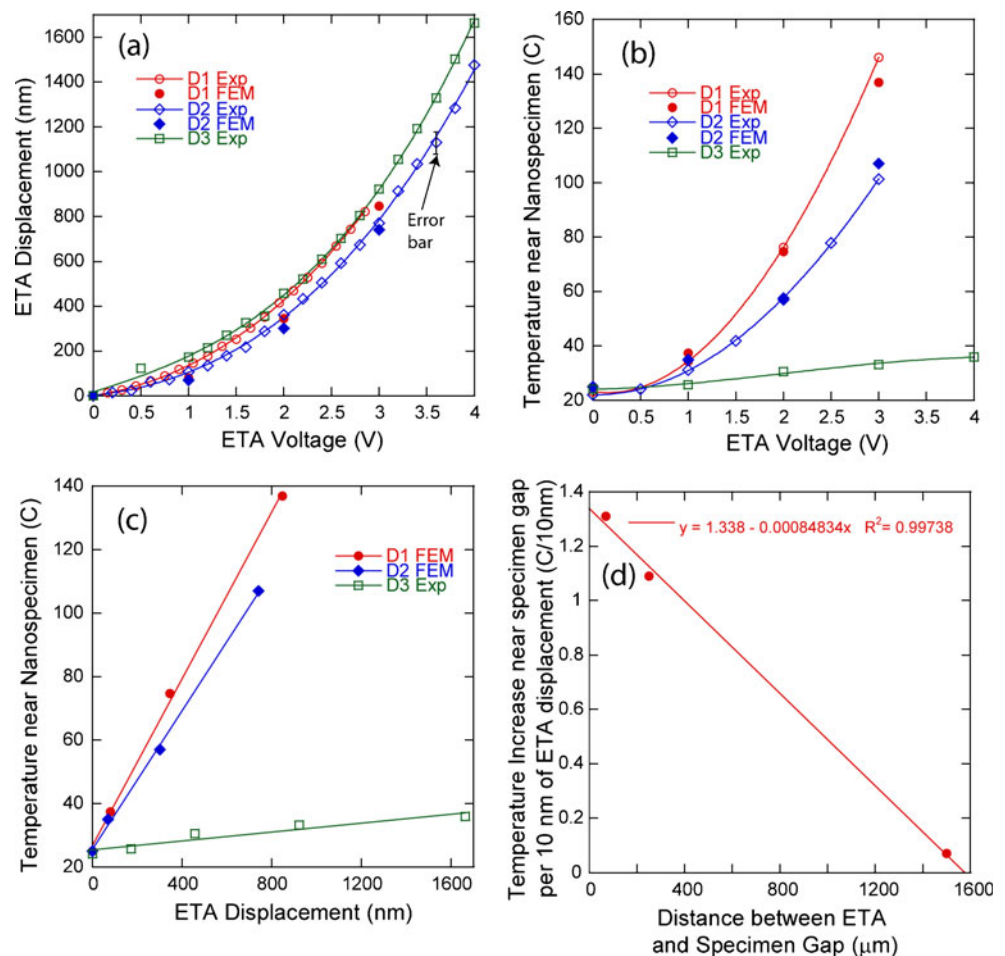

and D2 devices, it is still small enough to fit in an electrical biasing TEM holder for *in-situ* TEM testing.

While all the experiments reported in this paper were performed in air, it is important to characterize the device behavior in vacuum for experiments performed inside a SEM or TEM chamber. This behavior was studied using our finite element model that accurately reproduced the experimental results in air. In vacuum, conductive heat transfer through the air film below the device, and convective heat transfer do not occur. The effect of varying the convective heat transfer coefficients for air between 10 and 100 $W.m^{-2}.K^{-1}$ resulted in less than 5% variation in the ETA displacement. Hence convective heat transfer does not play a significant role compared to heat conduction. Figure 5 shows the temperature near the nanospecimen *vs.* ETA displacement for FEM simulations of the D1 MEMS device with and without heat conduction through the air film below the device. The predicted behavior in air and vacuum is similar, with nearly identical increases in temperature for a given ETA displacement. We therefore conclude that the D3 MEMS devices can also be operated in a SEM or TEM chamber and provide large actuator displacements (up to 1.6 μm) without any significant increase in temperature (<10°C).

Effect of Load Sensor Beams on Thermal Actuator Behavior

Figure 6 shows the load sensor stiffnesses calculated via finite element modeling, as a function of load sensor beam
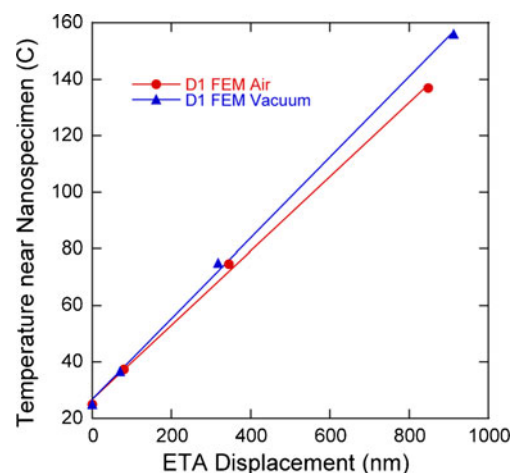
Fig. 5 Temperature near nanospecimen *vs.* ETA displacement for FE simulations performed in air and vacuum

Fig. 6 Stiffnesses calculated via FEM for two types of load sensors, assuming both small ("linear") and large ("non-linear") displacements: **a** 9-μm-wide beams; **b** 21-μm-wide beams. The lines highlight the different trends between linear and nonlinear FEM results
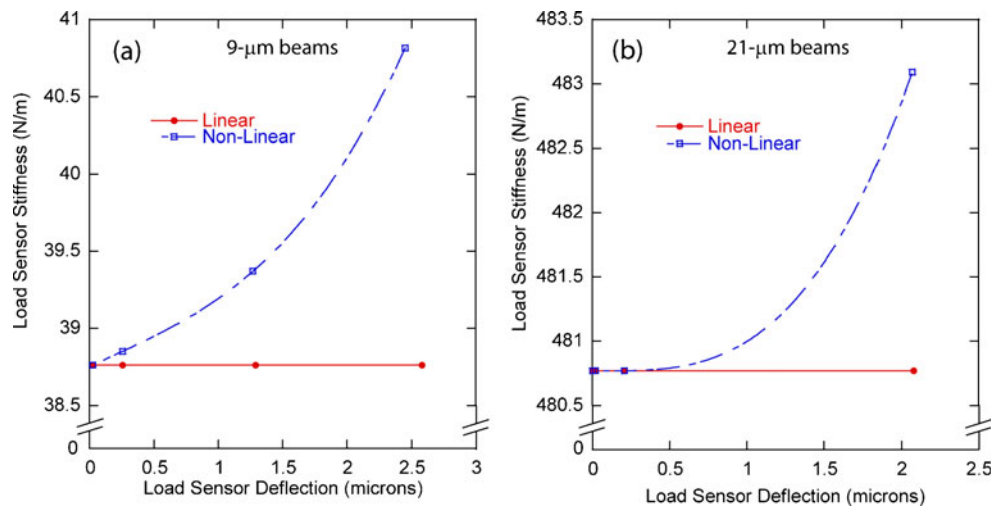
deflection, for the 9-μm-wide beams (Fig. 6(a)) and 21-μm-wide beams (Fig. 6(b)). The linear stiffnesses are 38.8 N/m and 481 N/m, respectively. For the 9-μm-wide (resp. 21-μm-wide beams), the non-linear stiffness is only 5% (resp. 0.5%) higher than the linear one for a total load sensor deflection of 2 μm. These nonlinear effects can therefore be ignored for force measurements.

As explained in the "Governing Equations of the MEMS Devices" section, the thermal actuator displacement X_A during a test may be different from the load-free displacement, $X_A^{F=0}$, if K_{LS} and K_S are not negligible compared to K_{TA}. The calculated thermal actuator stiffness is $K_{TA}=$ 3,760 N/m, according to equations (5) and (6). Hence, based on equation (4), we have:
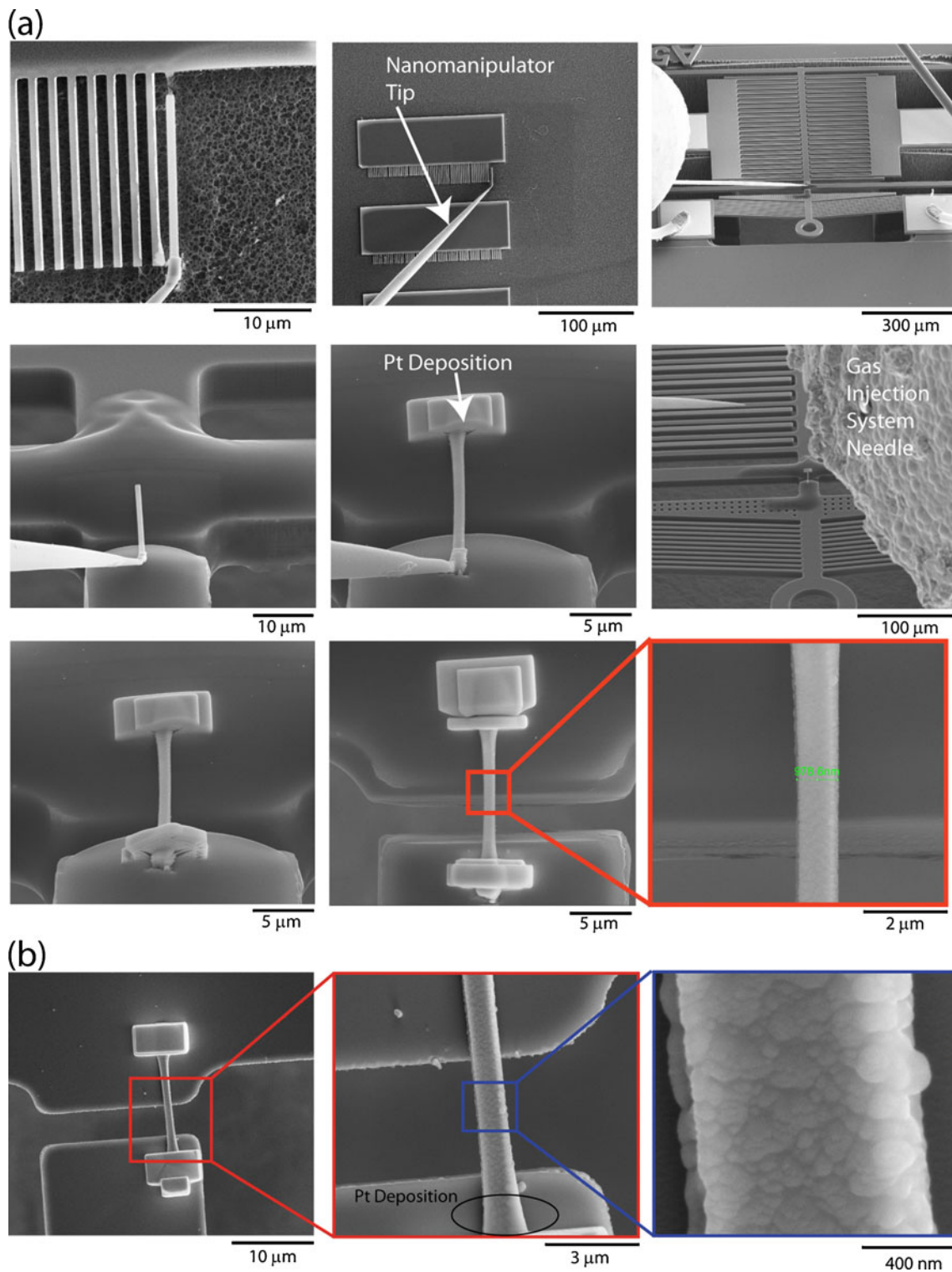
$$X_A = 0.99 X_A^{F=0} \quad \text{for a test with a 38.8N/m load sensor} \quad (7)$$

and

$$X_A = 0.89 X_A^{F=0} \quad \text{for a test with a 481 N/m load sensor} \quad (8)$$

Fig. 7 **(a)** Top down SEM images of the nanocrystalline Au nanobeams; **(b)** SEM images of the nanocrystalline Ni nanobeams viewed at an angle
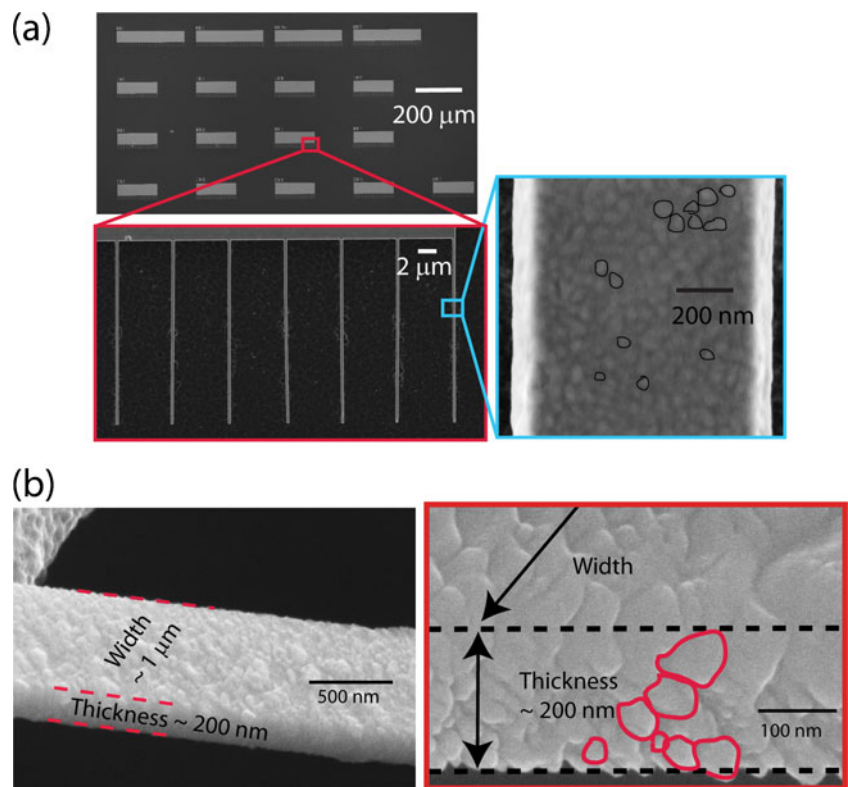
Fig. 8 (a) Sequence of SEM images showing nanobeam manipulation and placement onto MEMS device with a dual beam instrument equipped with a nanomanipulator. (b) An example of another Ni nanobeam clamped onto a MEMS device with Pt

The effect of the load sensor on X_A was experimentally verified by filling a specimen gap with stiff epoxy glue for a D3 MEMS device with a 481 N/m load sensor. At 4 V, the measured displacement was $X_A = 1540 \pm 50$ nm, while the load-free displacement was $X_A^{F=0} = 1660 \pm 50$ nm. The calculated ratio $X_A/X_A^{F=0}$ is 0.93 and is only 4% higher than equation (8).
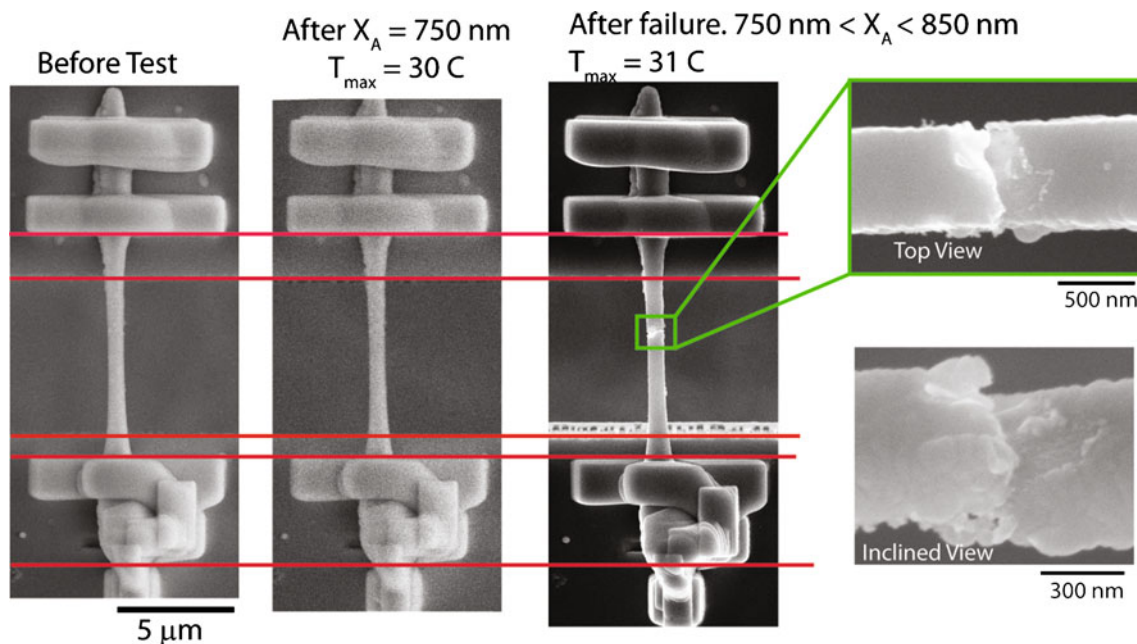
Tensile Testing of a Nanocrystalline Ni Nanobeam with D3 MEMS Device

The last section of this paper highlights some key aspects of the experimental procedure employed for the tensile testing of nanocrystalline nanobeams, using the D3 MEMS devices [32]. Both Ni and Au nanocrystalline nanobeams were fabricated using a process involving electron-beam lithography, electron-beam evaporation, lift-off technique, and XeF_2 release. At the end of the process, the nanobeams are free-standing and clamped on one side to a large island of metal (see Fig. 7(a)). Their dimensions are 10 or 20 µm long, 250 to 1,000 nm wide and ~200 nm thick. First, e-beam lithography (using a JEOL JBX-9300FS EBL system) is performed on a positive resist (PMMA A7) that is spin coated on a Si substrate. The photoresist is then developed in a methyl isobutyl ketone, isopropyl alcohol (MIBK:IPA) 1:1 solution. A thin Ni or Au film is then deposited on the patterned photoresist (using a CHA electron beam evaporator; deposition rate 2 Å/s, pressure at deposition start 2.5×10^{-7}— 4×10^{-7} Torr), followed by the removal of the photoresist (using 1,165 resist remover). This lift-off technique leads to nanoscale patterns of Ni or Au on the Si substrate, consisting of arrays of nanobeams attached to a large island of metal. Finally, the nanobeams are released from the substrate using XeF_2 as an isotropic etchant of Si (using a Xactix XeF_2 etcher). The etch time is such that about 1–2 µm of Si is etched away, which is sufficient to release the nanobeams without releasing the large islands. Figure 7(b) shows top down SEM images of Au nanobeams, as well as inclined SEM images of Ni nanobeams. The nanobeams are

nanocrystalline, with a few grains through the thickness. Grain size ranges from ~10 to 20 nm at the bottom to ~100 nm at the top.

The specimens can be manipulated and deposited onto the MEMS device using a FEI Nova Nanolab 200 dual beam (FIB/SEM) instrument, equipped with a gas injection system for ion-assisted platinum (Pt) deposition and a Kleindiek Nanotechnik MM3A micromanipulator (see Fig. 8). The micromanipulator tip is positioned near the free end of a nanobeam. Pt is then deposited to attach the micromanipulator tip to the nanobeam. The other end of the nanobeam (attached to the large Ni island) is milled off using FIB. The micromanipulator tip with the nanostructure is then positioned on the MEMS device across the specimen gap. The free end of the nanobeam is clamped to one side of the specimen gap using Pt deposition. The other end of the nanobeam is milled off of the micromanipulator tip (using FIB), and is also clamped using Pt deposition. Only a small section of the nanobeam (~1–2 µm) next to the large Pt clamps is coated with Pt (see Fig. 8(b)), while the largest part of the beam's length (>10 µm) is free of any Pt coating, as suggested by the high magnification SEM image in Fig. 8(b).

Figure 9 shows SEM images of a nanocrystalline Ni nanobeam before and after test, for which the electrical measurements and resulting stress–strain curve can be found in [32]. The specimen failed for a thermal actuator displacement, X_A, between 750 and 850 nm. According to Fig. 4(c), the resulting increase in temperature near the nanobeam is between 5 and 6°C. A D1 or D2 device would have resulted in a temperature increase between 100 and 110°C (D1) or 80 and 90°C (D2). Clearly, the improved

Fig. 9 Top down SEM images of a nanocrystalline Ni nanobeam, after testing to a series of imposed displacements with a D3 MEMS device

performance of the D3 device enables tensile tests at nearly constant temperature for this type of nanostructures. Another important advantage of the D3 device is the possibility to measure specimen elongation electrically with sub-nm resolution,[3] thanks to the 2 capacitive sensors surrounding the nanospecimen [32]. As such, the testing procedure does not require *in-situ* SEM or TEM testing to measure specimen elongation from high magnification images, enabling the possibility to investigate environmental effects on the mechanical properties of nanostructures.

Conclusion

In conclusion, we have presented an electrothermal-actuator-based MEMS device that can perform tensile tests at nearly constant temperature (room temperature) for a large range of nanomaterials. This MEMS device exhibit an increase in temperature near the specimen gap of only 0.07°C per 10 nm displacement of the thermal actuator, compared to ~2°C per 10 nm for previously reported electro-thermal-actuator-based MEMS devices. This improved performance appears to be directly related to the larger distances between thermal actuator and specimen gap, as highlighted by our characterization of 3 MEMS designs. We also presented an experimental procedure to measure the tensile properties of nanocrystalline nanobeams, which rely on the manipulation and attachment of these nanobeams onto the MEMS device inside a dual beam instrument.

An ideal testing setup for studying thermally activated phenomena in nanomaterials should include a controlled heating capability, independent of the deformation imposed to the specimen. Such capability may be achieved with additional features to the current MEMS device (*e.g.*, micro-heaters) and should be further investigated.

References

1. Agrawal R, Peng B, Espinosa HD (2009) Experimental-computational investigation of ZnO nanowires strength and fracture. Nano Lett 9(12):4177–4183
2. Agrawal R, Peng B, Gdoutos EE, Espinosa HD (2008) Elasticity size effects in ZnO nanowires-A combined experimental-computational approach. Nano Lett 8(11):3668–3674
3. Peng B, Locascio M, Zapol P, Li SY, Mielke SL, Schatz GC, Espinosa HD (2008) Measurements of near-ultimate strength for multiwalled carbon nanotubes and irradiation-induced crosslinking improvements. Nat Nanotechnol 3(10):626–631
4. Richter G, Hillerich K, Gianola DS, Monig R, Kraft O, Volkert CA (2009) Ultrahigh Strength Single Crystalline Nanowhiskers Grown by Physical Vapor Deposition. Nano Lett 9(8):3048–3052
5. Desai AV, Haque MA Mechanical properties of ZnO nanowires. In, 2007. Elsevier Science Sa, pp 169–176.
6. Zhang DF, Breguet JM, Clavel R, Philippe L, Utke I, Michler J (2009) *In situ* tensile testing of individual Co nanowires inside a scanning electron microscope. Nanotechnology 20(36):365706
7. Zhang DF, Breguet JM, Clavel R, Sivakov V, Christiansen S, Michler J (2010) Electron microscopy mechanical testing of silicon nanowires using electrostatically actuated tensile stages. J Microelectromech Sys 19(3):663–674
8. Greer JR, Nix WD (2005) Size dependence of mechanical properties of gold at the sub-micron scale. Appl Phys a-Mater Sci Process 80(8):1625–1629
9. Greer JR, Nix WD (2006) Nanoscale gold pillars strengthened through dislocation starvation. Physical Review B 73(24)
10. Greer JR, Oliver WC, Nix WD (2005) Size dependence of mechanical properties of gold at the micron scale in the absence of strain gradients. Acta Materialia 53(6):1821–1830
11. Kim J-Y, Greer JR (2009) Tensile and compressive behavior of gold and molybdenum single crystals at the nano-scale. Acta Materialia 57(17):5245–5253
12. Kim J-Y, Jang D, Greer JR (2009) Insight into the deformation behavior of niobium single crystals under uniaxial compression and tension at the nanoscale. Scr Mater 61(3):300–303
13. Philippe L, Wang Z, Peyrot I, Hassel AW, Michler J (2009) Nanomechanics of rhenium wires: elastic modulus, yield strength and strain hardening. Acta Materialia 57(14):4032–4035
14. Brown JJ, Suk JW, Singh G, Baca AI, Dikin DA, Ruoff RS, Bright VM (2009) Microsystem for nanofiber electromechanical measurements. Sens Actuator A-Phys 155(1):1–7
15. Wu B, Heidelberg A, Boland JJ (2005) Mechanical properties of ultrahigh-strength gold nanowires. Nat Mater 4(7):525–529
16. Shan ZW, Mishra RK, Asif SAS, Warren OL, Minor AM (2008) Mechanical annealing and source-limited deformation in submicrometre-diameter Ni crystals. Nat Mater 7(2):115–119
17. Haque MA, Saif MTA (2004) Deformation mechanisms in freestanding nanoscale thin films: a quantitative *in situ* transmission electron microscope study. Proc Natl Acad Sci United States America 101(17):6335–6340
18. Lu SN, Guo ZY, Ding WQ, Dikin DA, Lee J, Ruoff RS (2006) In situ mechanical testing of templated carbon nanotubes. Rev Sci Instrum 77(12):125101
19. Ostlund F, Rzepiejewska-Malyska K, Leifer K, Hale LM, Tang YY, Ballarini R, Gerberich WW, Michler J (2009) Brittle-to-ductile transition in uniaxial compression of silicon pillars at room temperature. Adv Funct Mater 19(15):2439–2444
20. Espinosa HD, Zhu Y, Moldovan N (2007) Design and operation of a MEMS-based material testing system for nanomechanical characterization. J Microelectromech Sys 16(5):1219–1231
21. Zhu Y, Corigliano A, Espinosa HD (2006) A thermal actuator for nanoscale *in situ* microscopy testing: design and characterization. J Micromech Microeng 16(2):242
22. Zhu Y, Espinosa HD (2005) An electromechanical material testing system for *in situ* electron microscopy and applications. Proc Natl Acad Sci United States America 102(41):14503–14508
23. Zhu Y, Moldovan N, Espinosa HD (2005) A microelectromechanical load sensor for *in situ* electron and X-ray microscopy tensile testing of nanostructures. Appl Phys Let 86(1):013506–013501

---

[3] We have not observed any permanent deformation or slippage of the Pt clamps (see Fig. 9) during tensile tests of nanobeams with applied forces up to 0.3–0.4 mN.

24. Ganesan Y, Lu Y, Peng C, Lu H, Ballarini R, Lou J (2010) Development and application of a novel microfabricated device for the *in situ* tensile testing of 1-D nanomaterials. J Microelectromech Sys 19(3):675–682

25. Lu Y, Ganesan Y, Lou J (2010) A multi-step method for *in situ* mechanical characterization of 1-D nanostructures using a novel micromechanical device. Exper Mech 50(1):47–54

26. Zhang DF, Drissen W, Breguet JM, Clavel R, Michler J (2009) A high-sensitivity and quasi-linear capacitive sensor for nanomechanical testing applications. J Micromech Microeng 19:075003

27. Lu SB, Guo ZY, Ding WQ, Ruoff RS (2006) Analysis of a microelectromechanical system testing stage for tensile loading of nanostructures. Rev Sci Instrum 77(5):056103

28. Lu SN, Dikin DA, Zhang SL, Fisher FT, Lee J, Ruoff RS (2004) Realization of nanoscale resolution with a micromachined thermally actuated testing stage. Rev Sci Instrum 75(6):2154–2162. doi:10.1063/1.1710703

29. Haque MA, Espinosa HD, Lee HJ (2010) MEMS for *in situ* testing-handling, actuation, loading, and displacement measurements. MRS Bull 35(5):375–381

30. Zhu T, Li J, Samanta A, Leach A, Gall K (2008) Temperature and strain-rate dependence of surface dislocation nucleation. Phys Rev Lett 100:025502

31. http://www.memscap.com/en_mumps.html (2010). www.memscap.com/memsrus/crmumps.html.

32. Pant B, Allen BL, Zhu T, Gall K, Pierron ON (2011) A versatile microelectromechanical system for nanomechanical testing. Appl Phys Let 98(5):053506

33. Beechem T, Graham S, Kearney SP, Phinney LM, Serrano JR (2007) Invited article: simultaneous mapping of temperature and stress in microdevices using micro-Raman spectroscopy. Rev Sci Instrum 78(6)

34. Huang QA, Lees NKS (1999) Analysis and design of polysilicon thermal flexure actuator. J Micromech Microeng 9(1):64–70

35. Mankame ND, Ananthasuresh GK (2001) Comprehensive thermal modelling and characterization of an electro-thermal-compliant microactuator. J Micromech Microeng 11(5):452–462

36. Brantley WA (1973) Calculated elastic constants for stress problems associated with semiconductors devices. J Appl Phys 44(1):534–535